
Article:
Krämer, Tobias, Chadwick, F. Mark, Macgregor, Stuart A. et al. (1 more author) (2023) Solid-State Confinement Effects in Selective exo-H/D Exchange in the Rhodium σ-Norbornane Complex [(Cy2PCH2CH2PCy2)Rh(η2:η2-C7H12)][BArF4]. HELVETICA CHIMICA ACTA. e202200154. ISSN: 0018-019X

https://doi.org/10.1002/hlca.202200154

---

doi.org/10.1002/hlca.202200154

RESEARCH ARTICLE

HELVETICA chimica acta

Solid-State Confinement Effects in Selective *exo*-H/D Exchange in the Rhodium σ-Norbornane Complex $[(Cy_2PCH_2CH_2PCy_2)Rh(\eta^2{:}\eta^2\text{-}C_7H_{12})][BAr^F{}_4]$

Tobias Krämer,*[a] F. Mark Chadwick,[b] Stuart A. Macgregor,*[c] and Andrew S. Weller[d]

[a] Department of Chemistry, Maynooth University, Maynooth, Co. Kildare, W23 F2H6 Ireland,
e-mail: tobias.kraemer@mu.ie

[b] Department of Chemistry, Molecular Sciences Research Hub, Imperial College London, 82 Wood Lane, W12 0BZ, UK

[c] Institute of Chemical Sciences, Heriot-Watt University, Edinburgh, EH14 4AS, Scotland,
e-mail: s.a.macgregor@hw.ac.uk

[d] Department of Chemistry, University of York, Heslington, York YO10 5DD, UK

Dedicated to the memory of Professor *Jack Dunitz*

Density functional theory calculations modelling selective *exo*-H/D exchange observed in the Rh σ-alkane complex $[(Cy_2PCH_2CH_2PCy_2)Rh(\eta^2{:}\eta^2\text{-}endo\text{-NBA})][BAr^F{}_4]$, **[1-NBA][BAr$^F{}_4$]**, are reported, where $Ar^F = 3,5\text{-}C_6H_3(CF_3)_2$ and NBA = norbornane, C_7H_{12}. Two models were considered *1*) an isolated molecular cation, **[1-NBA]$^+$** and *2*) a full model in which **[1-NBA][BAr$^F{}_4$]** is treated in the solid state through periodic DFT. After an initial *endo*-*exo* rearrangement, both models predict H/D exchange to proceed through D_2 addition and oxidative cleavage followed by a rate-limiting C–H activation of the norbornane through a σ-CAM step to form a **[1-Rh(D)(η^2-HD)(norbornyl)]$^+$** intermediate. HD rotation followed by a σ-CAM C–D bond formation, HD reductive coupling and HD loss then complete the H/D exchange process. *exo*-H/D exchange is facilitated by a supporting agostic interaction and is consistently more accessible kinetically than the potentially competing *endo*-H/D exchange (isolated cation: $\Delta G^{\ddagger}_{exo} = +15.9$ kcal/mol, $\Delta G^{\ddagger}_{endo} = +18.4$ kcal/mol; solid state: $\Delta G^{\ddagger}_{exo} = +22.1$ kcal/mol, $\Delta G^{\ddagger}_{endo} = +25.1$ kcal/mol). The solid-state environment has a significant impact on the computed energetics, with barriers increasing by *ca.* 7 kcal/mol, while only the solid-state model correctly predicts the *endo*-bound NBA complex to be the resting state of the system. These outcomes reflect solid-state confinement effects within the pocket occupied by the **[1-NBA]$^+$** cation and defined by the *pseudo*-octahedral array of neighbouring $[BAr^F{}_4]^-$ anions. The asymmetry of the solid-state environment also requires a second H/D exchange pathway to be defined to account for reaction at all four *exo*-C–H bonds. These entail slightly higher barriers ($\Delta G^{\ddagger}_{exo} = +24.8$ kcal/mol, $\Delta G^{\ddagger}_{endo} = +27.5$ kcal/mol) but retain a distinct preference for *exo*- over *endo*-H/D exchange.

Keywords: C–H activation, confinement, H/D exchange, density functional theory calculations, mechanism, periodic-DFT, rhodium, σ-alkane complexes.

Introduction

σ-Alkane complexes are key intermediates in C–H activation processes,[1] and, as a result, much effort has been dedicated to characterising these species.[2,3] In solution, the low polarizability and sterically hindered nature of aliphatic C–H bonds means that alkanes are

Supporting information for this article is available on the WWW under https://doi.org/10.1002/hlca.202200154

poor ligands at transition metal centres, and are readily displaced by solvent, counterions or entropically favoured agostic interactions. Thus, although σ-alkane complexes have been observed directly in solution, produced through photolysis of metal-carbonyl precursors, or protonation of metal-alkyls, they are generally of limited stability, with short half-lives even at the very low temperatures used for their spectroscopic characterisation (see *Scheme 1,A*).[4–8] These factors have frustrated attempts to isolate σ-alkane complexes in the solid state and their definitive[9] crystallographic characterisation through recrystallization from solution has so far proved elusive. Indirect evidence for the existence of σ-alkane complexes is also seen in the observation of H/D exchange processes at the metal-bound carbon in alkyl deuterides, $L_nM(CH_2R)(D)$.[10] This implies the intermediacy of σ-alkane complexes formed through C–D reductive coupling, that, upon rearrangement, allow C–H oxidative cleavage to give the exchanged $L_nM(CHDR)(H)$ product (*Scheme 1,B*). The α-selectivity signals that the transient alkane ligand remains bound to the metal centre throughout and rules out alternative reductive elimination/oxidative addition mechanisms. Related to this, the observation of inverse kinetic isotope effects for alkane reductive elimination can be understood in terms of an initial C–H/C–D reductive coupling to form an intermediate alkane complex. This relatively favours the perdeuterated alkane, providing an inverse equilibrium isotope effect prior to rate limiting, but isotopically less sensitive, alkane elimination.[10]

Over the last decade the *Weller* group have developed alternative strategies to generate σ-alkane complexes directly in the solid state using solid-state molecular organometallic (SMOM) chemistry.[11,12] This exploits the reaction of H_2 gas with crystalline samples of cationic Rh-alkene precursor complexes, $[L_2Rh(alkene)][BAr^F{}_4]$, where L_2 is a bidentate phosphine and $Ar^F = 3,5\text{-}C_6H_3(CF_3)_2$. When such reactions proceed as a single-crystal to single-crystal (SC–SC) transformation[13] they produce the corresponding alkane complexes directly in a form amenable to crystallographic characterisation.[14] The most robust Rh σ-alkane complex produced to date through this route is $[(Cy_2PCH_2CH_2PCy_2)Rh(\eta^2{:}\eta^2\text{-NBA})][BAr^F{}_4]$ (**[1-NBA][BAr$^F{}_4$]**; NBA = norbornane, C_7H_{12}) formed by hydrogenation of its $[(Cy_2PCH_2CH_2PCy_2)Rh(\eta^2{:}\eta^2$-

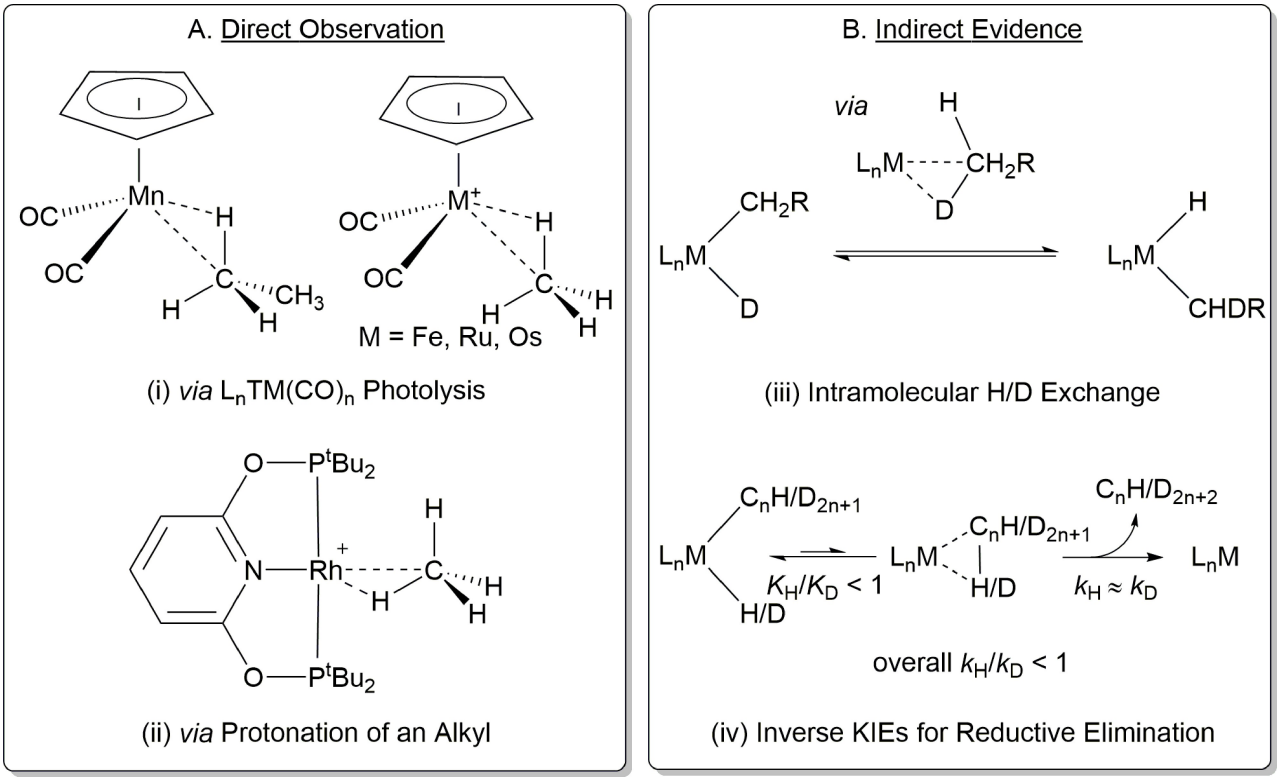

Scheme 1. A) Recent examples of direct observation of σ-alkane complexes in solution formed through (i) photolysis and (ii) alkyl protonation (anions omitted).[4–7] B) Indirect evidence for σ-alkane complexes: (iii) selective α-H/D *via* σ-alkane complex intermediates and (iv) inverse k_H/k_D isotope effects on alkane reductive elimination.[10]

NBD)][BAr$^F_4$] precursor (**[1-NBD][BAr$^F_4$]**; NBD = norbornadiene, C_7H_8, *Figure 1,A*).[15] This SC–SC transformation is complete within five minutes and forms a σ-complex in which the NBA ligand is bound through two adjacent *endo*-C–H bonds that both interact in an η^2-C–H fashion. **[1-NBA][BAr$^F_4$]** is stable for months under an inert atmosphere. Key to this stability is the rigid network of [BAr$^F_4$]$^-$ anions that form a *pseudo*-octahedral array around the Rh cation (*Figure 1,B*). Within this the NBA ligand lies confined in a V-shaped cavity defined by the neighbouring [BAr$^F_4$]$^-$ anion (*Figure 1,C*). Analogous SC–SC reactivity has been extended to form σ-complexes of other cyclic alkanes (cyclohexane,[16] cyclooctane[17]) and an array of linear and branched alkanes.[18] Variations of the anion,[19,20] chelating phosphine[15,17,21,22] and extension to a paramagnetic Co-NBA complex[23] have also been reported. The CF_3-groups in the [BAr$^F_4$]$^-$ anions are also suggested to play an important role in the ingress of gaseous reactants, and the egress of products, through the crystalline lattice, by providing hydrophobic nonporous channels.[24]

The SMOM chemistry of σ-alkane complexes has also been extended to reactivity studies in the solid state and these have also been supported by computational studies.[25] Examples include alkane fluxionality[16,26,27] and substitution,[12] as well as room temperature alkane dehydrogenation[16] and H/D exchange reactions.[16,27] These last two processes directly link σ-alkane complexes to C–H bond activation events. For **[1-NBA][BAr$^F_4$]** a particularly well-defined set of H/D exchange processes was characterised in the crystalline solid state, with neutron diffraction studies showing both the initial hydrogenation and subsequent H/D exchange to be highly selective (*Scheme 2*).[27] Thus exposure of **[1-NBD][BAr$^F_4$]** to D_2 forms **[1-(*endo*-D$_4$-NBA)][BAr$^F_4$]** showing both D_2 molecules are installed on the *endo* face of the alkane. Prolonged exposure to D_2 then forms **[1-(*exo,endo*-D$_8$-NBA)][BAr$^F_4$]** where H/D exchange has occurred at all four *exo*-C–H bonds. Exposure of this species to H_2 then selectively regenerates the *endo*-D_4 complex. These H/D exchange reactions complement, and provide a counterpoint to, the equivalent solution phase reactivity. In particular, in the solid state it is the σ-alkane complex that has been directly observed with alkyl hydride intermediates being inferred through H/D exchange, whereas in solution the reverse is usually the case, with the alkyl hydrides being observed.

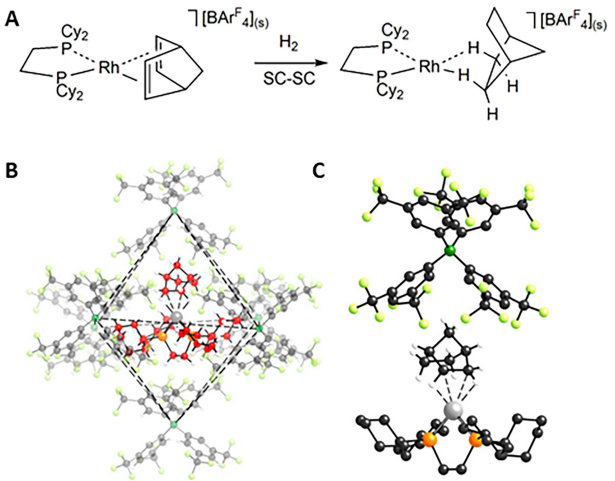

Figure 1. A) Synthesis of **[1-NBA][BAr$^F_4$]** by hydrogenation of **[1-NBD][BAr$^F_4$]** through a solid/gas single-crystal to single-crystal (SC–SC) methodology. B) Packing diagram showing arrangement of the six closest [BAr$^F_4$]$^-$ anions to the [1-NBA]$^+$ cation. C) **[1-NBA][BAr$^F_4$]** ion-pair showing the position of the NBA ligand within the cavity defined by the proximate [BAr$^F_4$]$^-$ anion.

This selectivity for H/D exchange at all four *exo*-C–H positions in **[1-NBA][BAr$^F_4$]** was puzzling, given the initial formation of the η^2,η^2-bis-*endo* bound isomer in which there are only two Rh···H–C interactions. In previous work the rearrangements of the bound NBA required for this selectivity, and to account for H/D exchange occurring at all four *exo*-C–H bonds, were modelled (see *Scheme 3*), and these studies highlighted the remarkable mobility of this ligand in the solid state.[27] Starting from the observed *endo*-bound isomer, **1$_{endo}$**, a 'rock' motion gives **1$_{exo}$** where Rh is bound to the C_1–H_{12} and C_2–H_{22} *exo*-C–H bonds. An alternative *exo*-bound structure, **1$_{exo\text{-}2}$**, can then be accessed through a 'tumble/wag' motion that moves the C_7 bridge from below to above the Rh coordination plane, whilst keeping the bridging methylene hydrogens intact. The lowest energy pathway to access the two remaining *exo*-C–H bonds proceeds through initial C_2 rotation of the NBA ligand to give **1$_{endo*}$** (*i.e.*, isostructural with **1$_{endo}$**, but now bound through the C_4–H_{41} and C_5–H_{51} *endo*-C–H bonds) from

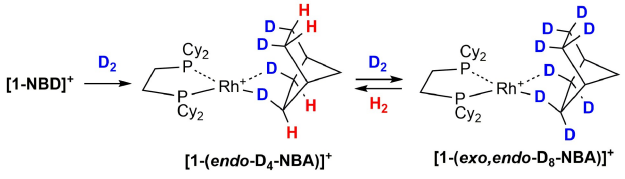

Scheme 2. Selective deuteration and H/D exchange processes in the **[1-NBD/NBA][BAr$^F_4$]** system (anions omitted).

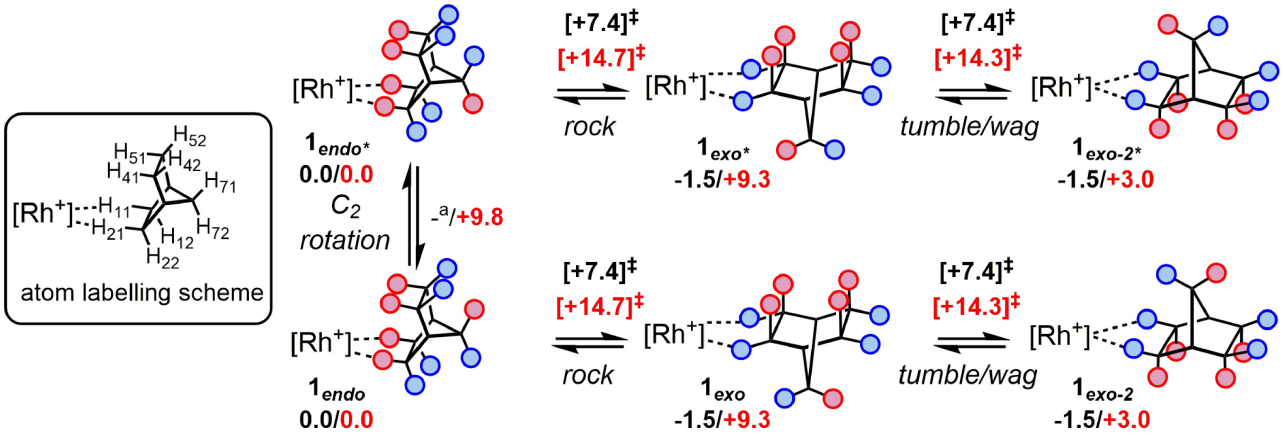

Scheme 3. Key rearrangements of the NBA ligand in **[1-NBA][BAr$^F_4$]** to access different *exo*-bound isomers, with computed relative free energies in kcal/mol and transition state energies in square brackets. Data in black are for the isolated cation model, **[1-NBA]$^+$**, and those in red are for **[1-NBA][BAr$^F_4$]** computed in the solid state through periodic DFT. The H-atom labelling scheme is also shown; [Rh$^+$] = [(Cy$_2$PCH$_2$CH$_2$PCy$_2$)Rh]$^+$. [a] C_2 rotation transition state could not be located with the isolated cation model.

which the 'rock' motion forms **1$_{exo*}$** bound through the C_4–H_{42} and C_5–H_{52} *exo*-C–H bonds. A 'tumble/wag' motion can then access **1$_{exo\text{-}2*}$**. Calculations on both the isolated **[1-NBA]$^+$** cation (the 'gas-phase') and periodic DFT calculations on **[1-NBA][BAr$^F_4$]** that include the extended crystal lattice highlighted the importance of the solid-state environment on the energetics of these processes.[25] Thus, for the isolated cation the *exo*-isomer is 1.5 kcal/mol more stable than the *endo*-form and the precise orientation of the NBA ligand relative to the [(Cy$_2$PCH$_2$CH$_2$PCy$_2$)Rh]$^+$ fragment has no effect on the energy with **1$_{exo}$** (with the C_7 bridge being 'down') and **1$_{exo\text{-}2}$** (C_7 bridge 'up') being coincidentally degenerate. In contrast, with periodic DFT **1$_{endo}$** is computed to be the most stable form, consistent with the crystal structure, and the degeneracy of **1$_{exo}$** and **1$_{exo\text{-}2}$** is lifted. These differences reflect the confinement of the NBA ligand within the array of adjacent [BAr$^F_4$]$^-$ anions that are now included in the periodic DFT model (*cf. Figure 1,B, C*).

While the above studies provide the necessary landscape of NBA rearrangements for the selective *exo*-H/D exchange in **[1-NBA][BAr$^F_4$]** to occur, the subsequent C–H activation processes have not yet been modelled, and it is this aspect that we address here. Several mechanistic possibilities can be envisaged for H/D exchange in this system, however, some additional experimental observations serve to narrow the field: *1*) exposure of single-crystals of **[1-(*exo,endo*-D$_8$-NBA)][BAr$^F_4$]** to H_2 results in the formation of HD; *2*) addition of HD to **[1-(*exo,endo*-H$_8$-NBA)][BAr$^F_4$]** leads to the formation of both the D_3 and D_4 isotopologues of the NBA ligand. Both observations imply Rh(III)-hydride/deuteride intermediates, while the latter outcome indicates H/D exchange must occur in a stepwise rather than a pairwise fashion, most likely through σ-complex-assisted metathesis (σ-CAM) processes.[28,29]

Two general mechanisms consistent with these observations are shown in *Scheme 4*. Starting from the *exo*-bound isomer, **1$_{exo}$**, *Pathway 1* involves norbornene intermediates such as **B** formed through activation of both *exo*-C–H bonds through C–H oxidative cleavage and β-H transfer. Addition of D_2 followed by H/D exchange, HD loss, migratory insertion and reductive coupling then generate the mono-deuterated product **1′$_{exo}$** (throughout, a prime (or double prime) will indicate an isotopologue formed through one (or more) H/D exchange processes). H_2/D_2 exchange at **B** through H_2 reductive elimination followed by D_2 oxidative addition can be ruled out as it would involve a pairwise H/D exchange. Alternatively, *Pathway 2* can be accessed *via* initial norbornyl intermediates such as **A** formed by a single C–H bond activation. **A** can then be intercepted by D_2 to form **D** which then undergoes H/D exchange to form **D′**. HD loss and C–H reductive coupling then leads to **1′$_{exo}$**. An equivalent set of pathways is possible for H/D exchange in **1$_{endo}$**.

Several factors can serve to complicate *Pathways 1* and *2* in *Scheme 4*. The sequence of events may vary; for example, **D** could be formed through **E** (D_2 addition then C–H activation). The *exo*- and *endo*-faces of the norbornane (or norbornyl/norbornene) ligands also give rise to several distinct geometries; for example, the addition of H_2 to **1$_{exo}$** can occur at either

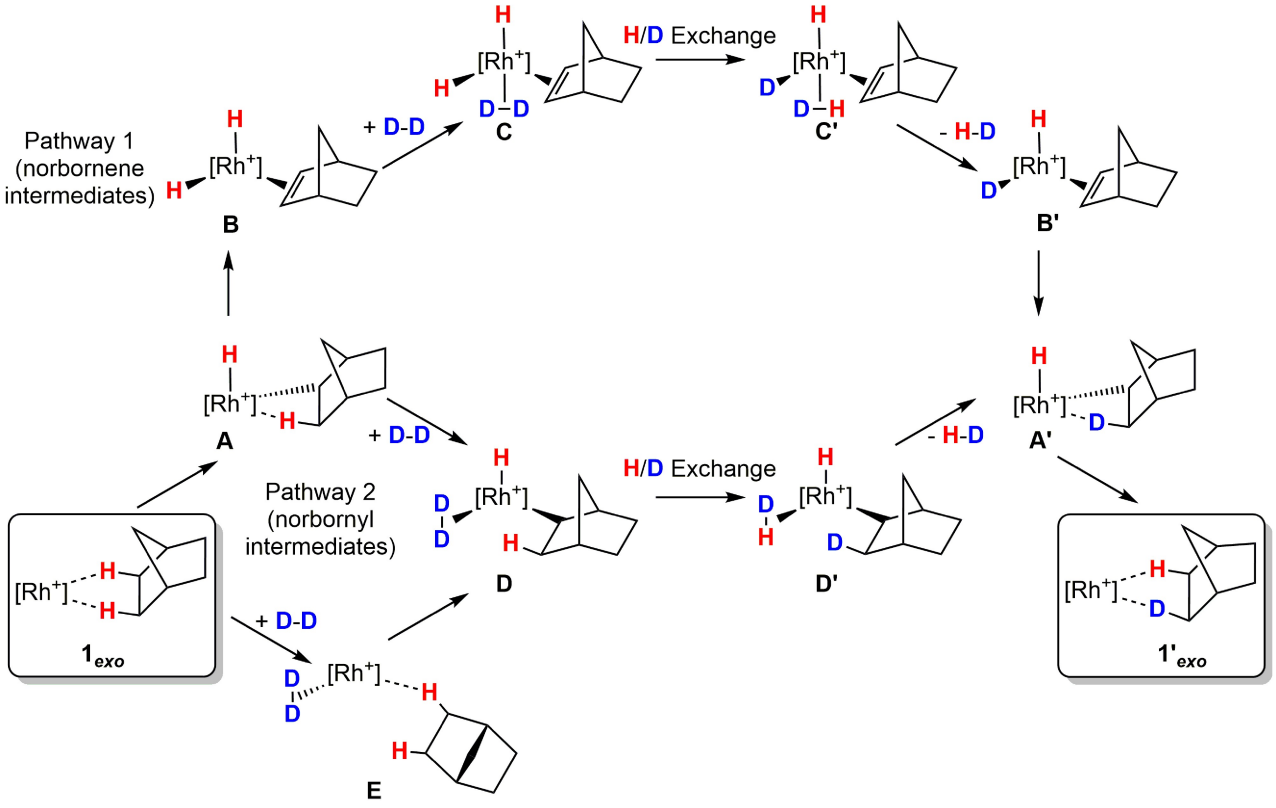

Scheme 4. General mechanisms for H/D exchange in **[1-NBA][BAr$^{F}_{4}$]**.

the *exo*- or *endo*-face of the NBA ligand, and with displacement of either the 'front' or 'back' C–H bond as viewed in *Scheme 4*. There are therefore four possibilities: in *Scheme 4*, the geometry of **E** reflects H_2 addition at the *exo*-face with displacement of the 'front' C–H bond. Addition to the *exo*-face is generally favoured as it rotates the C_7 methylene bridge of the NBA ligand away from the Cy substituents of the phosphine backbone. The H/D exchange steps also present different variations; for example, D_2 activation through a
σ-CAM in **D** may occur with either the hydride or the alkyl ligand. All these possibilities were explored to define the most accessible H/D exchange pathways in both $\mathbf{1}_{exo}$ and $\mathbf{1}_{endo}$ with the aim of accounting for the *exo*-selectivity seen experimentally.

Results and Discussion

Isolated Cation Model, [1-NBA]$^+$

Initial calculations considered H/D exchange in the isolated cation. Calculations on this model are useful to explore the intrinsic behaviour of the system and so focus the computationally more demanding periodic DFT calculations on the most relevant pathways. A comparison of the isolated cation and the extended periodic models also allows the effects of the solid-state environment to be quantified. The PBE–D3 functional in conjunction with double-ζ plus polarization-quality basis sets were employed throughout for both the molecular and the periodic DFT calculations; we have shown this approach reproduces the structures of σ-alkane complexes in the solid state, as well as experimental barriers for fluxional and alkane dehydrogenation processes[25] (see the *Supporting Information* for full details of methodology). In the following the isolated cation model will be signalled by a positive charge in the labelling of stationary points (*e.g.*, $\mathbf{1}^{+}_{exo}$, $\mathbf{1}^{+}_{endo}$, *etc.*), whereas neutral labels will signify the full model computed in the solid state with periodic DFT that fully represents the extended crystalline environment (*e.g.*, $\mathbf{1}_{exo}$, $\mathbf{1}_{endo}$, *etc.*)

The most accessible H/D exchange processes for $\mathbf{1}^{+}_{exo}$ are shown in *Scheme 5* (details of alternative mechanisms are given in the *Supporting Information*, see *Figures S1–S4*). Along *Pathway 1*, $\mathbf{1}^{+}_{exo}$ readily undergoes C–H oxidative cleavage and β-H transfer to

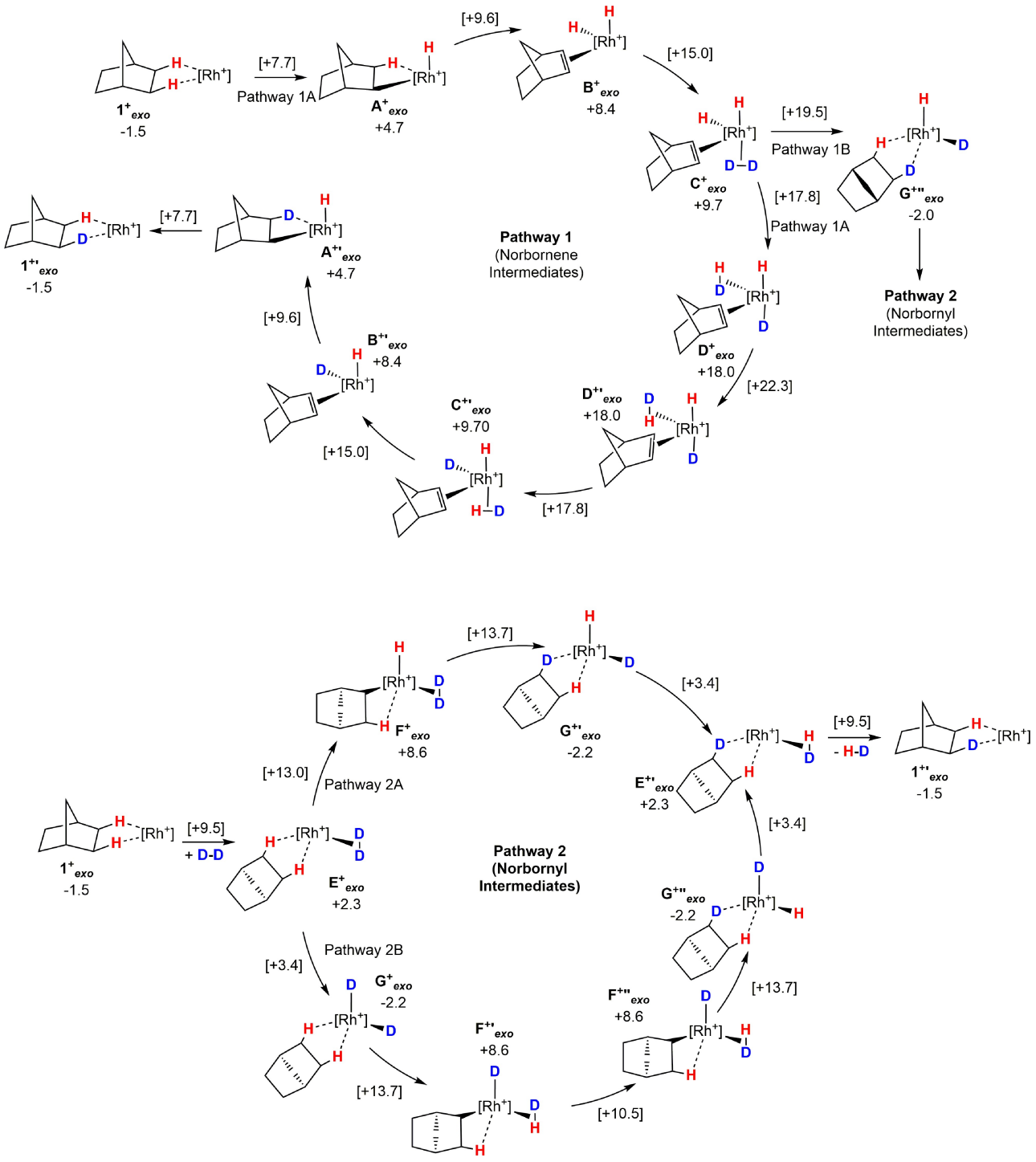

Scheme 5. Computed lowest energy pathways for *exo*-C–H H/D exchange in $\mathbf{1}^{+}_{exo}$. Free energies are indicated in kcal/mol with transition state energies in square brackets.

give square-pyramidal **[1-Rh(H)$_2$(NBE)]$^+$**, $\mathbf{B}^{+}_{exo}$, at +8.4 kcal/mol. D_2 addition then forms $\mathbf{C}^{+}_{exo}$ from which *Pathway 1A* proceeds with D_2 activation through a σ-CAM to form **[1-Rh(η^2-HD)(D)(H)(NBE)]$^+$**, $\mathbf{D}^{+}_{exo}$ (+18.0 kcal/mol), with trans H and D ligands. HD rotation then gives $\mathbf{D}^{+\prime}_{exo}$ from which the microscopic reverse steps (σ-CAM, HD loss, migratory insertion, and C–H reductive coupling) lead to the H/D exchanged product $\mathbf{1}^{+\prime}_{exo}$. The rate-limiting transition state along *Pathway 1A* is the HD rotation step

($\mathbf{D^+}_{exo} \rightarrow \mathbf{D^{+\prime}}_{exo}$) at +22.3 kcal/mol, the high energy of which reflects the trans-dihydride arrangement in these species. Alternatively, $\mathbf{C^+}_{exo}$ can also react along *Pathway 1B* through D-transfer from the η^2-D_2 ligand onto the norbornene. This was found to induce C–H reductive coupling with one of the hydride ligands to form $\mathbf{G^{+\prime\prime}}_{exo}$ that was then shown to be an intermediate along *Pathway 2B*. As the subsequent steps involving $\mathbf{G^{+\prime\prime}}_{exo}$ are facile (see below) *Pathway 1B* is the most accessible route involving a norbornene intermediate with an overall barrier relative to $\mathbf{1}_{exo}^+$ of 21.0 kcal/mol.

Along *Pathway 2*, D_2 addition displaces one Rh···H–C σ-interaction to form **[1-Rh(η^2-D_2)(norbornane)]$^+$** ($\mathbf{E^+}_{exo}$, +2.3 kcal/mol). *Pathway 2A* then proceeds through C–H oxidative cleavage to give $\mathbf{F^+}_{exo}$ followed by a σ-CAM D_2 activation to form $\mathbf{G^{+\prime}}_{exo}$. HD reductive elimination through $\mathbf{E^{+\prime}}_{exo}$ forms $\mathbf{1^{+\prime}}_{exo}$. Alternatively, *Pathway 2B* involves oxidative cleavage of D_2 in $\mathbf{E^+}_{exo}$ to give $\mathbf{G^+}_{exo}$. H/D exchange then occurs through a σ-CAM C–H activation to $\mathbf{F^{+\prime}}_{exo}$, HD rotation to $\mathbf{F^{+\prime\prime}}_{exo}$ and a σ-CAM to generate $\mathbf{G^{+\prime\prime}}_{exo}$. HD reductive elimination through $\mathbf{E^{+\prime}}_{exo}$ again forms $\mathbf{1'}_{exo}$. The rate-limiting transition states along both *Pathways 2A* and *2B* correspond to D_2 activation through a σ-CAM step with an energy of +13.7 kcal/mol (*i.e.*, $\mathbf{F^+}_{exo} \rightarrow \mathbf{G^{+\prime}}_{exo}$ along *Pathway 2A* or $\mathbf{G^+}_{exo} \rightarrow \mathbf{F^{+\prime}}_{exo}$ (and $\mathbf{F^{+\prime\prime}}_{exo} \rightarrow \mathbf{G^{+\prime\prime}}_{exo}$) along *Pathway 2B*). Thus, for the isolated cation model *Pathway 2* involving norbornyl intermediates is clearly favoured over *Pathway 1* with norbornene intermediates. In all cases, the most energetically demanding steps involve Rh(III) species, either HD rotation in $\mathbf{D^+}_{exo}$ (*Pathway 1A*), D_2 activation in $\mathbf{C^+}_{exo}$ (*Pathway 1B*), or D_2 activation in $\mathbf{F^+}_{exo}$ (*Pathways 2A/2B*).

Repeating these calculations for H/D exchange in the *endo* isomer, $\mathbf{1^+}_{endo}$, provided an analogous set of *Pathways 1A/1B* and *2A/2B* (see *Figures S5–S8*). In each case, the highest lying transition state is equivalent to that characterised for H/D exchange in $\mathbf{1^+}_{exo}$. However, the *endo* structures are consistently higher in energy than their *exo*-analogues: *Pathway 1A*, $\mathbf{D^+}_{endo} \rightarrow \mathbf{D^{+\prime}}_{endo}$ (+26.3 kcal/mol); *Pathway 1B*, $\mathbf{C^+}_{endo} \rightarrow \mathbf{G^{+\prime}}_{endo}$ (+27.2 kcal/mol); *Pathways 2A* and *2B*, $\mathbf{G^+}_{endo} \rightarrow \mathbf{F^{+\prime}}_{endo}/\mathbf{F^{+\prime\prime}}_{endo} \rightarrow \mathbf{G^{+\prime\prime}}_{endo}$ (+17.1 kcal/mol). The kinetic preference for *exo*-H/D exchange in the norbornane ligand is therefore already present in the isolated cation model. *Figure 2,A* compares *Pathway 2B* for the *exo*- and *endo*-isomers and shows these diverge at the C–H activation step ($\mathbf{G^+} \rightarrow \mathbf{F^+}$) for which the transition state is 3.4 kcal/mol lower along the *exo*-pathway. A similar difference is maintained in the isomers of $\mathbf{F^+}$ and the H_2 rotation transition state before the pathways return to near parity after C–H coupling ($\mathbf{F^{+\prime}} \rightarrow \mathbf{G^{+\prime}}$). Comparison of the C–H activation transition state structures (*Figure 2,B*) shows the *exo* form, **TS($\mathbf{G^+}_{exo}$–$\mathbf{F^+}_{exo}$)**, features a somewhat stronger agostic interaction (Rh···H_{12} = 1.97 Å; C_1–H_{12} = 1.17 Å) than in **TS($\mathbf{G^+}_{endo}$–$\mathbf{F^+}_{endo}$)** (Rh···H_{11} = 2.05 Å; C_1–H_{11} = 1.15 Å). In addition, a short H_{21}···H_{41} contact of 1.89 Å is seen in **TS($\mathbf{G^+}_{endo}$–$\mathbf{F^+}_{endo}$)**, well below the sum of the *van der Waals* radii (2.42 Å[30]). The shortest such contact involving the transferring H in **TS($\mathbf{G^+}_{exo}$–$\mathbf{F^+}_{exo}$)** is 2.42 Å (H_{22}···H_{72}). Similar σ-CAM C–H activation transition states[1] have also been reported recently as part of a study of norbornene hydrogenation at a pincer-type [P_2Si]Rh complex.[31]

For both H/D exchange processes the isomers of **[1-Rh(D)$_2$(NBA)]$^+$**, $\mathbf{G^+}_{exo}$ and $\mathbf{G^+}_{endo}$, are the most stable species and the overall barriers relative to these are 15.9 kcal/mol and 19.4 kcal/mol for *exo*- and *endo*-H/D exchange, respectively. This trend therefore captures the preference for *exo*-H/D exchange, however, the size of these barriers would suggest both processes should be accessible at room temperature, while only *exo*-H/D exchange is seen experimentally. Moreover, the computed stability of Rh(III) dihydrides $\mathbf{G^+}_{exo}$ and $\mathbf{G^+}_{endo}$ contradicts experiment where only the *endo*-bound form of Rh(I) **[1-NBA][BAr$^F_4$]** is observed. The isolated cation model therefore does not capture the full experimental behaviour and so we turned to periodic DFT to take the effects of the solid-state environment into account.

Solid-State Model

In addition to the various mechanistic possibilities described above, another key factor in the solid state is the orientation of the NBA moiety within the pocket defined by the framework of $[BAr^F_4]^-$ anions. *Figure 3* shows the adjacent ion-pairs computed for $\mathbf{1}_{endo}$, $\mathbf{1}_{exo}$

[1] The transition state for migratory insertion in [(P_2Si)Rh-(H)$_2$(NBE)]$^+$ is 11.2 kcal/mol lower for the *exo*-isomer. This is equivalent to **TS($\mathbf{B^+}_{exo}$-$\mathbf{A^+}_{exo}$)** in the present study which is more stable than the *endo* equivalent by 7 kcal/mol. This preference is likely due to the proximity of the *endo*-C–H bonds to the bulky P_2Si and dcype ligands that are enforced by the more rigid binding mode of the norbornene ligand. In contrast, the rate limiting transition states here – **TS($\mathbf{G^+}_{exo}$–$\mathbf{F^+}_{exo}$)** and **TS($\mathbf{G^+}_{endo}$–$\mathbf{F^+}_{endo}$)** – show similar short contacts between the norbornyl and substituents of the supporting phosphine ligand and so steric effects do not seem to be a distinguishing factor.

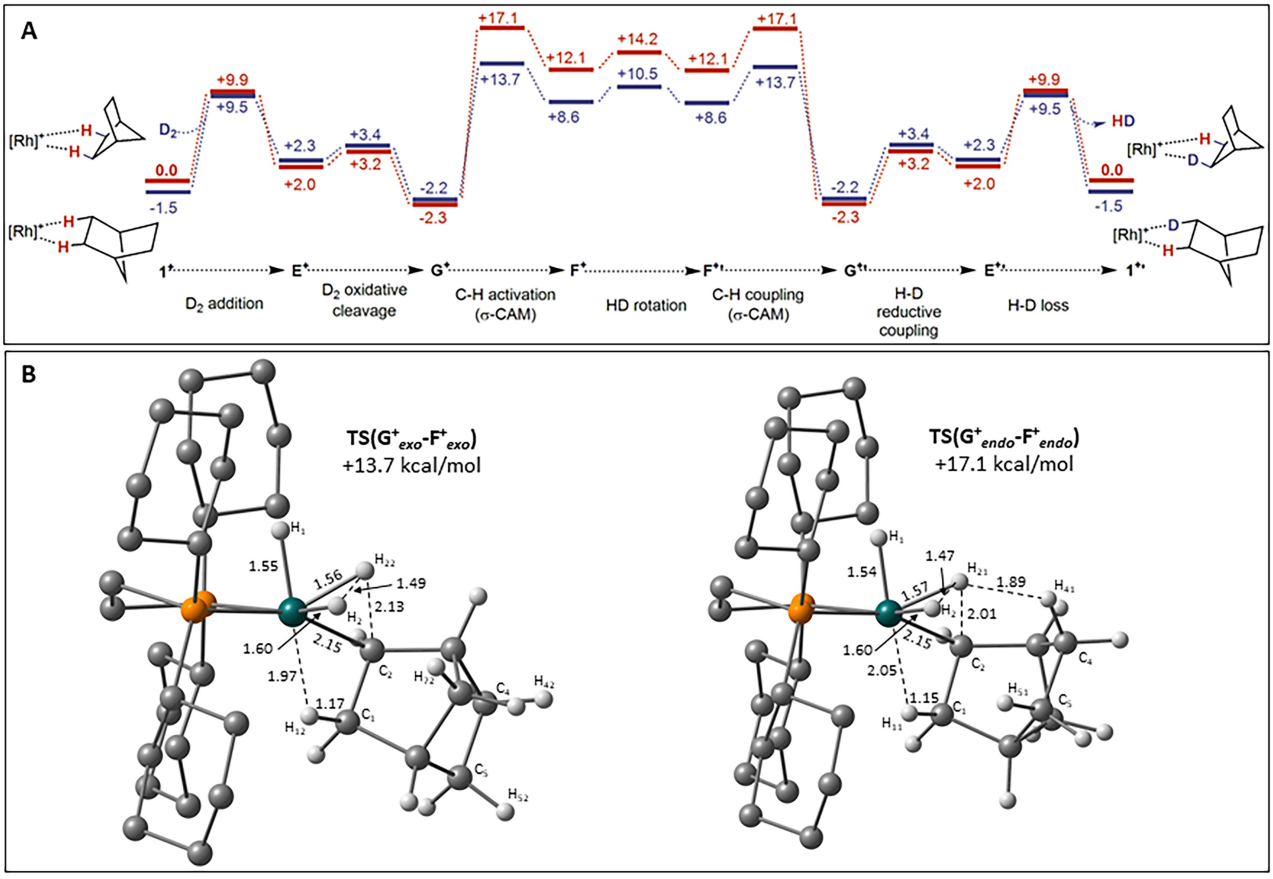

Figure 2. A). Computed free energy profiles comparing H/D exchange in $\mathbf{1}^{+}_{exo}$ and $\mathbf{1}^{+}_{endo}$. B) Details of the computed σ-CAM transition state structures, **TS(G^{+}–F^{+})**, for *exo*- and *endo*-C–H bond activation with selected distances in Å.

and $\mathbf{1}_{exo\text{-}2}$ as defined in *Scheme 3*. In $\mathbf{1}_{endo}$, the **[1-NBA]$^{+}$** cation is slightly skewed relative to the anion such that the distance of the B-atom from the PRhP plane, d, is 1.50 Å and the PRhP/$C_{aryl}BC_{aryl}$ interplane angle, ϕ, is 4.0°. Rearrangement to $\mathbf{1}_{exo\text{-}2}$ is accommodated with little change in these metrics (d = 1.48 Å; ϕ = 2.9°). In contrast, for $\mathbf{1}_{exo}$ the B-atom lies slightly below the PRhP plane (d = 0.05, ϕ = −5.4°) and this change reflects a tilting of the **[1-NBA]$^{+}$** to avoid a steric clash with the lower half of the anion. This then comes at an energetic cost such that $\mathbf{1}_{exo}$ is 6.3 kcal/mol less stable than $\mathbf{1}_{exo\text{-}2}$. More generally, structures that involve moving the NBA moiety into the lower sector of the ion-pair pocket are found to be disfavoured.

Exo-H/D exchange can initiate from either $\mathbf{1}_{exo}$ or $\mathbf{1}_{exo\text{-}2}$ (*Scheme 6*) and will proceed through displacement of either the 'front' or the 'back' Rh···H–C σ-interaction by D_2 such that the NBA rotates to move the C_7 methylene bridge away from the Cy substituents of the diphosphine ligand.[2] This gives rise to four possibilities and in each case a mechanism corresponding to *Pathway 2B* was characterised in which the rate-limiting transition state is associated with the σ-CAM C–H activation step, **G** to **F**. The two most accessible pathways ($\Delta G^{\ddagger}$ = 22.1 kcal/mol and 24.8 kcal/mol) both originate from $\mathbf{1}_{exo}$ despite the higher energy of that species (+9.3 kcal/mol) compared to $\mathbf{1}_{exo\text{-}2}$ (+3.0 kcal/mol). The corresponding transition states are accessible as they involve rotation of the NBA moiety into the space above the Rh coordination plane (*i.e.*, the resulting ϕ values are positive). In contrast, H/D exchange pathways from $\mathbf{1}_{exo\text{-}2}$ have significantly higher barriers of 35.9 kcal/mol and 39.6 kcal/mol as D_2 addition to the *exo*-face

[2] D_2 addition at the *endo*-face of either $\mathbf{1}_{exo}$ or $\mathbf{1}_{endo}$ forces rotation of the NBA towards the Cy substituents and gives structures that are either very high in energy or do not correspond to local minima.

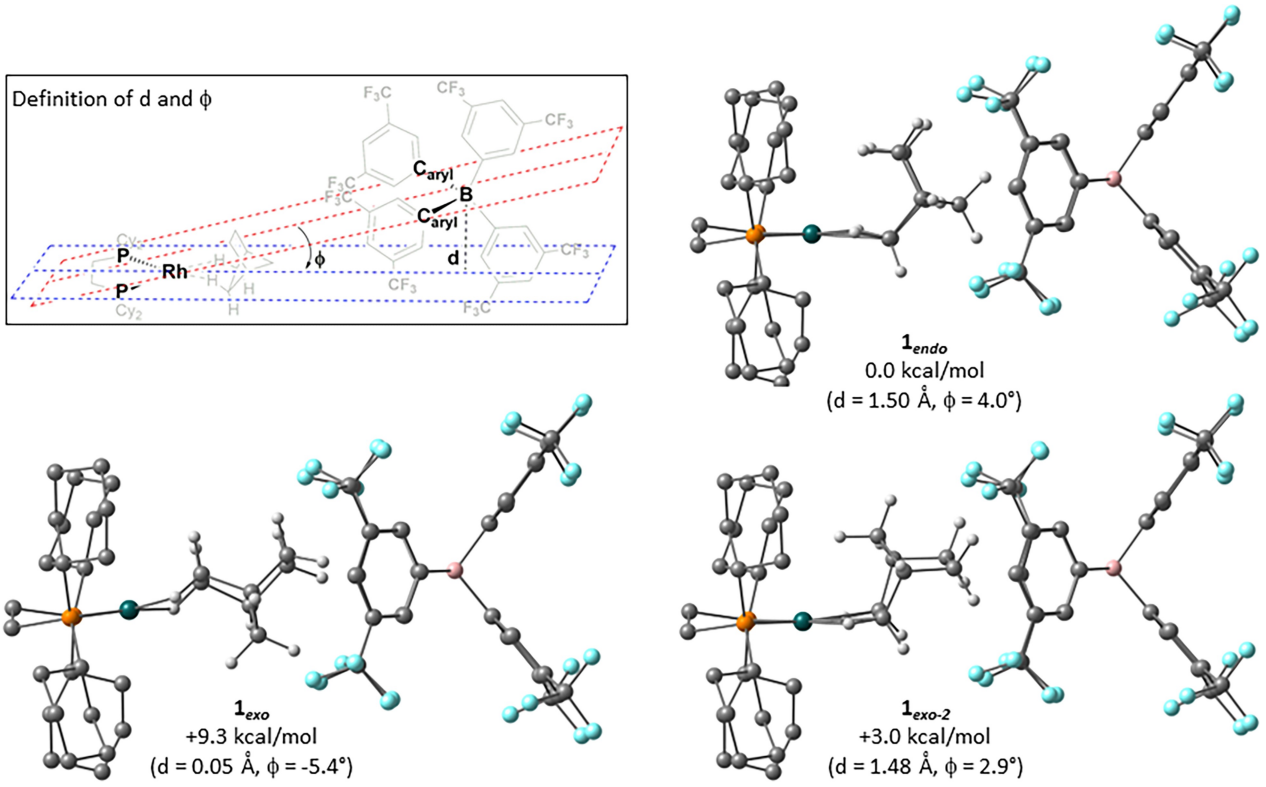

Figure 3. Computed structures, relative free energies and metrics, (d and ϕ, as defined) for adjacent ion-pairs in $\mathbf{1}_{endo}$, $\mathbf{1}_{exo}$ and $\mathbf{1}_{exo\text{-}2}$. Non-NBA H-atoms are omitted for clarity.

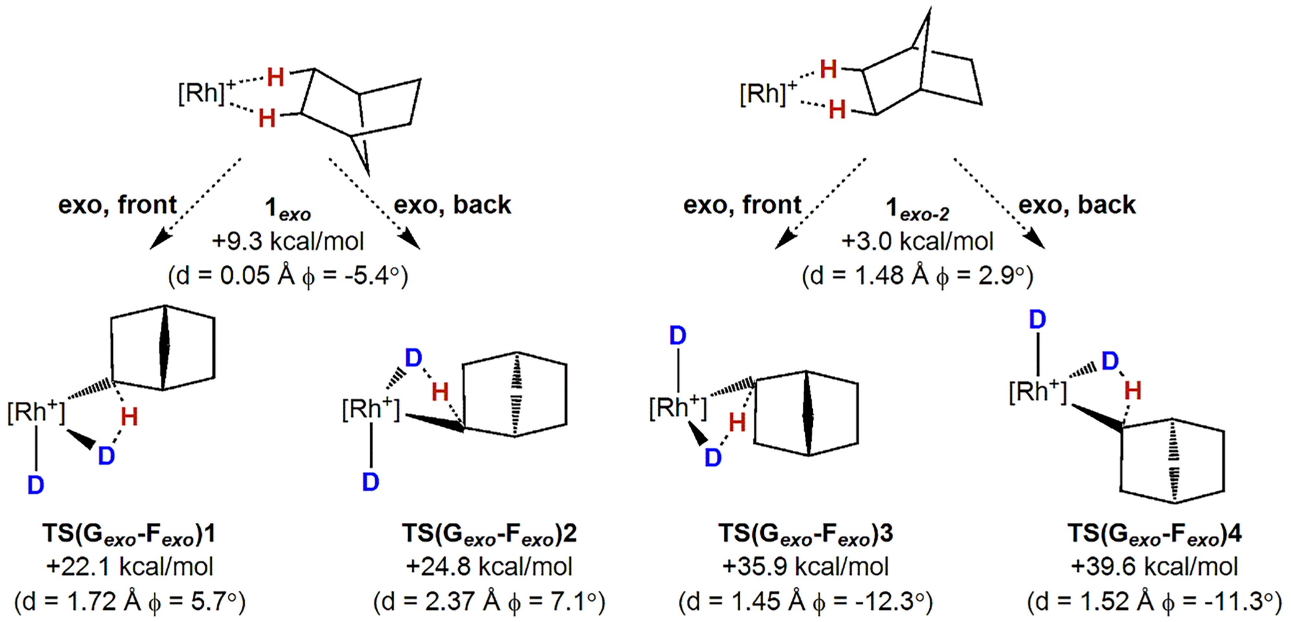

Scheme 6. Schematic representation of the fours variants of the rate-limiting transition state, **TS(G_{exo}–F_{exo})**, formed through addition of D_2 to the *exo*-faces of $\mathbf{1}_{exo}$ and $\mathbf{1}_{exo\text{-}2}$. Relative free energies computed with periodic DFT in the solid state and the key metrics, d and ϕ, are also provided.

rotates the NBA moiety below the Rh coordination plane, forcing an upward tilt of the Rh cation within the pocket (ϕ values are negative). Similar considerations for the *endo*-isomer showed the most accessible pathway originated from the crystallographically observed structure, $\mathbf{1}_{endo}$ (0.0 kcal/mol) with an overall barrier of 25.1 kcal/mol (see *Figure S10*).

The lowest energy mechanisms for both *exo*- and *endo*-H/D exchange in the solid state are compared in *Figure 4,A*. In each case rate-limiting C–H activation in **G** forms **[1-Rh(H)(η²-HD)(C_7H_{11})][BAr^F_4]**, **F**, which upon HD rotation, accesses the microscopic reverse C–D coupling to form **[1-Rh(H)(D)(C_7H_{11}D)][BAr^F_4]**, **G′**. *exo*-H/D exchange therefore follows *Curtin–Hammett* kinetics with an initial 'rock' rearrangement from the $\mathbf{1}_{endo}$ resting state to form $\mathbf{1}_{exo}$ at +9.3 kcal/mol (*Scheme 3*) preceding rate-limiting H/D exchange. The overall barriers of 22.1 kcal/mol for *exo*-H/D exchange and 25.1 kcal/mol for *endo*-H/D exchange in the solid state are both *ca.* 7 kcal/mol higher than in the isolated cation model and are therefore more in line with the experimentally observed reactivity. The periodic DFT calculations therefore capture the *exo*-selectivity for H/D exchange; moreover, $\mathbf{1}_{endo}$ is now computed to be the most stable species in the system, consistent with this being the sole species observed experimentally.

The computed distances associated with the σ-CAM process in **TS(G_{exo}–F_{exo})1** are very similar to those computed with the isolated cation (compare *Figures 2,B* and *4,B*). The increased barriers in the solid state are therefore likely to arise from the steric impact of the neighbouring [BAr^F_4]⁻ anions. This can be seen in the close approach of the C_4–C_5 ethylene unit of the norbornyl ligand towards one of the aryl substituents of the neighbouring [BAr^F_4]⁻ anion. Further support for this is seen in the *Hirshfeld* surface (*Figure 4,C*) where the red areas signify short $H_{norbornyl}\cdots C_{aryl}$ contacts below the sum of the *van der Waals* radii. The reasons for the *exo*-selectivity being

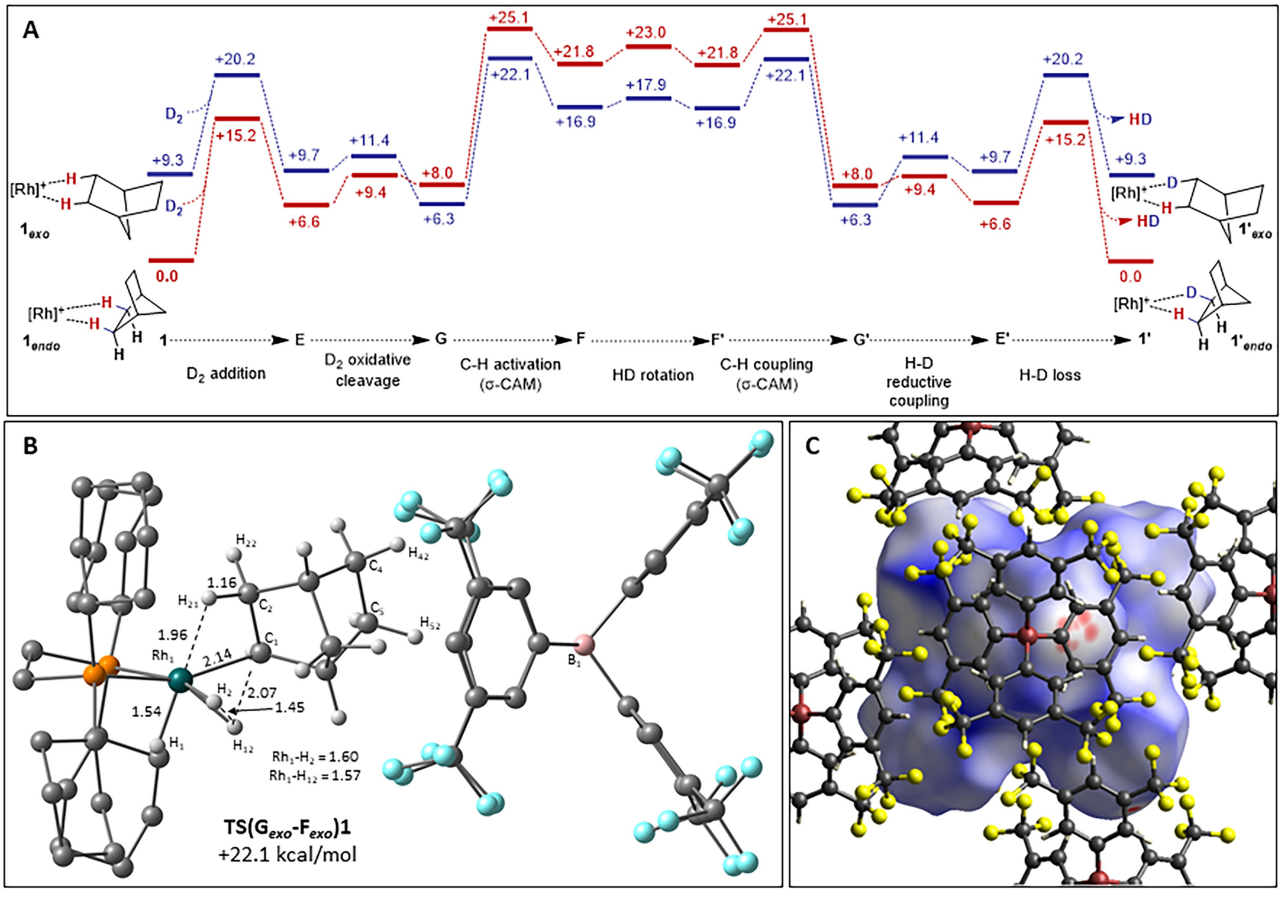

Figure 4. A) Computed free energy profiles comparing H/D exchange in $\mathbf{1}_{endo}$ and $\mathbf{1}_{exo}$. B) Details of the computed σ-CAM transition state structures, **TS(G_{exo}–F_{exo})1** showing the reacting Rh cation and the adjacent [BAr^F_4]⁻ anion. C) *Hirshfeld* surface for **TS(G_{exo}–F_{exo})1** mapped over d_{norm} for the reacting Rh cation placed within the surrounding *pseudo*-octahedron of [BAr^F_4]⁻ anions. The surface is viewed down the $Rh_1\cdots B_1$ vector.

maintained in the solid state are more subtle. This arises in part from the easier C–H activation step, as noted above for the isolated cation, and the computed transition states again show a greater agostic interaction involving the C_2–H_{21} bond in the *exo*-isomer. However, this effect is smaller in the solid state ($\Delta\Delta G^{\ddagger}_{\mathbf{G}\rightarrow\mathbf{F}} = 1.3$ kcal/mol) and an additional contribution comes from the greater stability of $\mathbf{G}_{exo}$ over $\mathbf{G}_{endo}$ ($\Delta G = 1.7$ kcal/mol).

Experimentally, H/D exchange occurs at all four *exo*-C–H bonds: both the C_1–H_{12} bond (as shown above) and the C_2–H_{22} bond interact with the Rh centre in $\mathbf{1}_{exo}$ and access to the C_4–H_{42} and C_5–H_{52} bonds is possible through rearrangement from $\mathbf{1}_{exo}$ to $\mathbf{1}_{exo*}$. This entails a C_2 rotation to interconvert the degenerate $\mathbf{1}_{endo}$ and $\mathbf{1}_{endo*}$ structures (see *Scheme 3*) meaning that the NBA ligand reacts with local C_2 symmetry such that the pairs of diagonally related C–H bonds are equivalent. C_1–H_{12} and C_4–H_{42} therefore both react through **TS($\mathbf{G}_{exo}$–$\mathbf{F}_{exo}$)1** at +22.1 kcal/mol, while the C_2–H_{22} and C_5–H_{52} bonds both react through **TS($\mathbf{G}_{exo}$–$\mathbf{F}_{exo}$)2** at +24.8 kcal/mol. Similar considerations for *endo*-H/D exchange provide higher computed barriers for the C_1–H_{11}/C_5–H_{51} and C_2–H_{21}/C_4–H_{41} bond pairs of +25.1 kcal/mol and +27.5 kcal/mol respectively. A summary of all these H/D exchange processes for $\mathbf{1}_{endo}$ is shown in *Figure 5*, where the NBA ligand is viewed from the Rh centre with the surrounding $[BAr^F{}_4]^-$ anions shown in space-filling mode. Overall *exo*-H/D exchange is always favoured, although the similar barriers to *exo*-H/D exchange in the C_2–H_{22}/C_5–H_{52} bond pair and *endo*-H/D exchange in the C_1–H_{11}/C_5–H_{41} pair are not consistent with the exclusive *exo*-H/D exchange seen experimentally. However, for a given methylene group the barrier to H/D exchange is always approximately 3 kcal/mol lower for the *exo*-C–H bond, consistent with a preference for reaction at the *exo*-position.

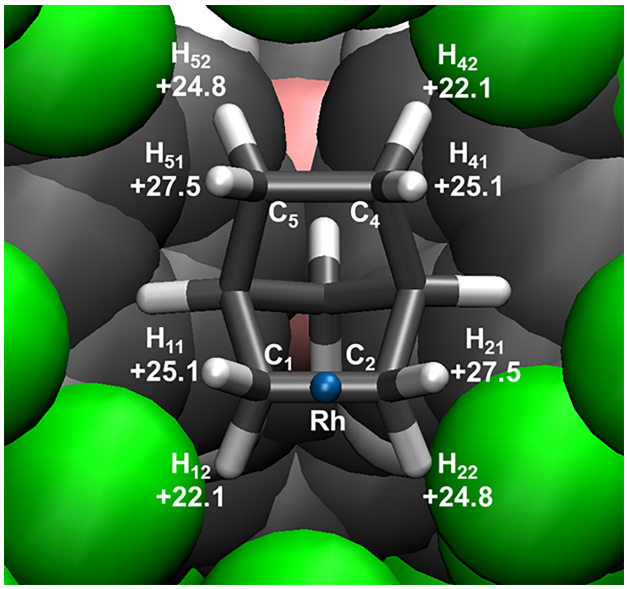

Figure 5. Summary of overall free energy barriers (kcal/mol) for H/D exchange at all four *exo*- and *endo*-C–H bonds in $\mathbf{1}_{endo}$. The NBA ligand is shown within the cavity formed by the surrounding anions (in space filling mode) and is viewed from the Rh atom (blue). Other atoms: B; pink; F: green; C: grey; H: white.

Conclusions

H/D exchange pathways for the Rh σ-alkane complex **[1-NBA][$BAr^F{}_4$]**, $\mathbf{1}_{endo}$, have been computed to model the selective *exo*-H/D exchange seen experimentally. Both an isolated cation model, **[1-NBA]$^+$**, and a full solid-state model computed through periodic DFT have been considered. For both models the lowest energy H/D exchange pathways proceed through initial D_2 addition and oxidative cleavage followed by rate-limiting C–H activation of the norbornane ligand through a σ-CAM process to give a **[1-(norbornyl)(D)(η^2-HD)]$^+$** intermediate. After HD rotation the microscopic reverse steps (σ-CAM C–D bond formation, HD reductive coupling and HD loss) complete the H/D exchange process. In both models the lowest energy *exo*-H/D exchange is more accessible than the competing *endo*-H/D exchange (isolated cation: $\Delta G^{\ddagger}_{exo} = +15.9$ kcal/mol, $\Delta G^{\ddagger}_{endo} = +18.4$ kcal/mol; solid state: $\Delta G^{\ddagger}_{exo} = +22.1$ kcal/mol, $\Delta G^{\ddagger}_{endo} = +25.1$ kcal/mol). We propose that a stronger supporting agostic interaction contributes to the lower energy of the rate-limiting σ-CAM transition state along the *exo*-H/D exchange pathways.

Although both models predict the same H/D exchange mechanism, the associated energetics differ significantly. Thus, the isolated cation model incorrectly predicts that the *exo*-bound form of σ-alkane complex is more stable than the observed *endo*-bound structure, and that the resting state of the system is the **[1-(NBA)$(D)_2$]$^+$** cation. These inconsistencies are corrected in the periodic DFT calculations that also give overall barriers to H/D exchange that are *ca.* 7 kcal/mol higher in energy. The larger barriers in the solid state reflect confinement effects within the pocket defined by the neighbouring $[BAr^F{}_4]^-$ anions, with several short contacts between the norbornyl ligand and an aryl ring of an adjacent anion being identified in the rate-limiting σ-CAM transition states.

The asymmetry of the solid-state pocket also adds significant complexity to the modelling of these systems with two separate pathways being required to account fully for H/D exchange at all four *exo*-C–H bonds. As seen in previous examples,[25] confinement effects play a key role in defining the structure and reactivity of these SMOM systems. This in turn offers the prospect of controlling reactivity through judicious design of the solid-state environment, a goal we are pursuing in current and future work.

Supporting Information

Supporting information for this article (computational methodologies and references, alternative computed reaction profiles, geometries and energies of all species) is available on the WWW under https://doi.org/hlca.202200154.

Acknowledgements

The EPSRC for funding through awards EP/K035908/1, EP/K035681/1 and EP/M024210/1.

Data Availability Statement

The data that support the findings of this study are available in the *Supporting Material* of this article.

Author Contributions Statement

F. M. C. and *A. S. W.* conceived and performed the experiments underpinning this study. *T. K.* and *S. A. M.* performed the calculations and manuscript writing. All authors contributed to the interpretation of results.

References

[1] J. F. Hartwig, 'Organotransition Metal Chemistry: From Bonding to Catalysis', University Science Books, Sausalito, **2010**.
[2] R. H. Crabtree, 'The Organometallic Chemistry of Alkanes', *Chem. Rev.* **1985**, *85*, 245–269.
[3] C. Hall, R. N. Perutz, 'Transition Metal Alkane Complexes', *Chem. Rev.* **1996**, *96*, 3125–3146.
[4] J. D. Watson, L. D. Field, G. E. Ball, 'Binding methane to a metal centre', *Nat. Chem.* **2022**, *14*, 801–804.
[5] J. D. Watson, L. D. Field, G. E. Ball, '$[Fp(CH_4)]^+$, $[\eta^5$-$CpRu(CO)_2(CH_4)]^+$, and $[\eta^5$-$CpOs(CO)_2(CH_4)]^+$: A Complete Set of Group 8 Metal–Methane Complexes', *J. Am. Chem. Soc.* **2022**, *144*, 17622–17629.
[6] W. H. Bernskoetter, C. K. Schauer, K. I. Goldberg, M. Brookhart, 'Characterization of a Rhodium(I) σ-Methane Complex in Solution', *Science* **2009**, *326*, 553–556.
[7] O. Torres, J. A. Calladine, S. B. Duckett, M. W. George, R. N. Perutz, 'Detection of σ-alkane complexes of manganese by NMR and IR spectroscopy in solution: $(\eta^5$-$C_5H_5)Mn(CO)_2$(ethane) and $(\eta^5$-$C_5H_5)Mn(CO)_2$(isopentane)', *Chem. Sci.* **2015**, *6*, 418–424.
[8] A. L. Pitts, A. Wriglesworth, X.-Z. Sun, J. A. Calladine, S. D. Zarić, M. W. George, M. B. Hall, 'Carbon–Hydrogen Activation of Cycloalkanes by Cyclopentadienylcarbonylrhodium – A Lifetime Enigma', *J. Am. Chem. Soc.* **2014**, *136*, 8614–8625.
[9] J. Jung, S. T. Löffler, J. Langmann, F. W. Heinemann, E. Bill, G. Bistoni, W. Scherer, M. Atanasov, K. Meyer, F. Neese, 'Dispersion Forces Drive the Formation of Uranium–Alkane Adducts', *J. Am. Chem. Soc.* **2020**, *142*, 1864–1870.
[10] W. D. Jones, 'Isotope Effects in C–H Bond Activation Reactions by Transition Metals', *Acc. Chem. Res.* **2003**, *36*, 140–146.
[11] A. S. Weller, F. M. Chadwick, A. I. McKay, 'Transition Metal Alkane-Sigma Complexes: Synthesis, Characterization, and Reactivity', Chapt. 5 in 'Advances in Organometallic Chemistry', Vol. 66, Ed. P. J. Pérez, Academic Press, 2016, pp. 223–276.
[12] F. M. Chadwick, A. I. McKay, A. J. Martínez-Martínez, N. H. Rees, T. Krämer, S. A. Macgregor, A. S. Weller, 'Solid-state molecular organometallic chemistry. Single-crystal to single-crystal reactivity and catalysis with light hydrocarbon substrates', *Chem. Sci.* **2017**, *8*, 6014–6029.
[13] K. A. Reid, D. C. Powers, '*In crystallo* organometallic chemistry', *Chem. Commun.* **2021**, *57*, 4993–5003.
[14] S. D. Pike, A. L. Thompson, A. G. Algarra, D. C. Apperley, S. A. Macgregor, A. S. Weller, 'Synthesis and Characterization of a Rhodium(I) σ-Alkane Complex in the Solid State', *Science* **2012**, *337*, 1648–1651.
[15] S. D. Pike, F. M. Chadwick, N. H. Rees, M. P. Scott, A. S. Weller, T. Krämer, S. A. Macgregor, 'Solid-State Synthesis and Characterization of σ-Alkane Complexes, $[Rh(L_2)(\eta^2,\eta^2$-$C_7H_{12})][BAr^{F4}]$ (L_2 = Bidentate Chelating Phosphine)', *J. Am. Chem. Soc.* **2015**, *137*, 820–833.
[16] A. I. McKay, A. J. Bukvic, B. E. Tegner, A. L. Burnage, A. J. Martínez-Martínez, N. H. Rees, S. A. Macgregor, A. S. Weller, 'Room Temperature Acceptorless Alkane Dehydrogenation from Molecular σ-Alkane Complexes', *J. Am. Chem. Soc.* **2019**, *141*, 11700–11712.
[17] A. J. Martínez-Martínez, B. E. Tegner, A. I. McKay, A. J. Bukvic, N. H. Rees, G. J. Tizzard, S. J. Coles, M. R. Warren, S. A. Macgregor, A. S. Weller, 'Modulation of σ-Alkane Interactions in $[Rh(L_2)(alkane)]^+$ Solid-State Molecular Organometallic (SMOM) Systems by Variation of the Chelating Phosphine and Alkane: Access to η^2,η^2-σ-Alkane Rh(I), η^1-σ-Alkane Rh(III) Complexes, and Alkane Encapsulation', *J. Am. Chem. Soc.* **2018**, *140*, 14958–14970.
[18] A. J. Bukvic, A. L. Burnage, G. J. Tizzard, A. J. Martínez-Martínez, A. I. McKay, N. H. Rees, B. E. Tegner, T. Krämer, H. Fish, M. R. Warren, S. J. Coles, S. A. Macgregor, A. S. Weller, 'A Series of Crystallographically Characterized Linear and Branched σ-Alkane Complexes of Rhodium: From Propane

to 3-Methylpentane', *J. Am. Chem. Soc.* **2021**, *143*, 5106–5120.
[19] L. R. Doyle, E. A. Thompson, A. L. Burnage, A. C. Whitwood, H. T. Jenkins, S. A. Macgregor, A. S. Weller, 'MicroED characterization of a robust cationic σ-alkane complex stabilized by the $[B(3,5\text{-}(SF_5)_2C_6H_3)_4]^-$ anion, *via* on-grid solid/gas single-crystal to single-crystal reactivity', *Dalton Trans.* **2022**, *51*, 3661–3665.
[20] A. I. McKay, A. J. Martínez-Martínez, H. J. Griffiths, N. H. Rees, J. B. Waters, A. S. Weller, T. Krämer, S. A. Macgregor, 'Controlling Structure and Reactivity in Cationic Solid-State Molecular Organometallic Systems Using Anion Templating', *Organometallics* **2018**, *37*, 3524–3532.
[21] S. K. Furfari, B. E. Tegner, A. L. Burnage, L. R. Doyle, A. J. Bukvic, S. A. Macgregor, A. S. Weller, 'Selectivity of Rh···H–C Binding in a σ-Alkane Complex Controlled by the Secondary Microenvironment in the Solid State', *Chem. Eur. J.* **2021**, *27*, 3177–3183.
[22] A. I. McKay, T. Krämer, N. H. Rees, A. L. Thompson, K. E. Christensen, S. A. Macgregor, A. S. Weller, 'Formation of a σ-alkane Complex and a Molecular Rearrangement in the Solid-State: $[Rh(Cyp_2PCH_2CH_2PCyp_2)(\eta^2\text{:}\eta^2\text{-}C_7H_{12})][BAr^F{}_4]$', *Organometallics* **2017**, *36*, 22–25.
[23] T. M. Boyd, B. E. Tegner, G. J. Tizzard, A. J. Martínez-Martínez, S. E. Neale, M. A. Hayward, S. J. Coles, S. A. Macgregor, A. S. Weller, 'A Structurally Characterized Cobalt(I) σ-Alkane Complex', *Angew. Chem. Int. Ed.* **2020**, *59*, 6177–6181.
[24] A. J. Martínez-Martínez, N. H. Rees, A. S. Weller, 'Reversible Encapsulation of Xenon and CH_2Cl_2 in a Solid-State Molecular Organometallic Framework (Guest@SMOM)', *Angew. Chem. Int. Ed.* **2019**, *58*, 16873–16877.
[25] A. G. Algarra, A. L. Burnage, M. Iannuzzi, T. Krämer, S. A. Macgregor, R. E. M. Pirie, B. Tegner, A. S. Weller, 'Computational Studies of the Solid-State Molecular Organometallic (SMOM) Chemistry of Rh σ-Alkane Complexes', in '21st Century Challenges in Chemical Crystallography II: Structural Correlations and Data Interpretation', Eds. D. M. P. Mingos, P. R. Raithby, Springer, Cham, 2020, pp. 183–228.
[26] F. M. Chadwick, N. H. Rees, A. S. Weller, T. Krämer, M. Iannuzzi, S. A. Macgregor, 'A Rhodium–Pentane Sigma-Alkane Complex: Characterization in the Solid State by Experimental and Computational Techniques', *Angew. Chem. Int. Ed.* **2016**, *55*, 3677–3681.
[27] F. M. Chadwick, T. Krämer, T. Gutmann, N. H. Rees, A. L. Thompson, A. J. Edwards, G. Buntkowsky, S. A. Macgregor, A. S. Weller, 'Selective C–H Activation at a Molecular Rhodium Sigma-Alkane Complex by Solid/Gas Single-Crystal to Single-Crystal H/D Exchange', *J. Am. Chem. Soc.* **2016**, *138*, 13369–13378.
[28] R. N. Perutz, S. Sabo-Etienne, 'The σ-CAM Mechanism: σ Complexes as the Basis of σ-Bond Metathesis at Late-Transition-Metal Centers', *Angew. Chem. Int. Ed.* **2007**, *46*, 2578–2592.
[29] R. N. Perutz, S. Sabo-Etienne, A. S. Weller, 'Metathesis by Partner Interchange in σ-Bond Ligands: Expanding Applications of the σ-CAM Mechanism', *Angew. Chem. Int. Ed.* **2022**, *61*, e202111462.
[30] S. Alvarez, 'A cartography of the van der Waals territories', *Dalton Trans.* **2013**, *42*, 8617–8636.
[31] M. T. Whited, M. J. Trenerry, K. E. DeMeulenaere, B. L. H. Taylor, 'Computational and Experimental Investigation of Alkene Hydrogenation by a Pincer-Type $[P_2Si]$Rh Complex: Alkane Release via Competitive σ-Bond Metathesis and Reductive Elimination', *Organometallics* **2019**, *38*, 1493–1501.

Received November 7, 2022
Accepted December 22, 2022

